

Passive array imaging in random media

Liliana Borcea and Ilker Kocyigit[‡]

February 4, 2022

Abstract

We present a novel algorithm for high resolution coherent imaging of sound sources in random scattering media using time resolved measurements of the acoustic pressure at an array of receivers. The sound waves travel a long distance between the sources and receivers so that they are significantly affected by scattering in the random medium. We model the scattering effects by large random wavefront distortions, but the results extend to stronger effects, as long as the waves retain some coherence i.e., before the onset of wave diffusion. It is known that scattering in random media can be mitigated in imaging using coherent interferometry (CINT). This method introduces a statistical stabilization in the image formation, at the cost of image blur. We show how to modify the CINT method in order to image wave sources that are too close to each other to be distinguished by CINT alone. We introduce the algorithm from first principles and demonstrate its performance with numerical simulations.

Keywords— Wave scattering in random media, coherent interferometric imaging, array imaging.

1 Introduction

Coherent array imaging is an important technology in radar [10], sonar [15], seismic imaging [2], photoacoustic imaging [16], medical imaging with ultrasound [18], and so on. We focus attention on passive array imaging, where a collection of N_r receivers record waves generated by N_s unknown sources. The receivers are located at points $\vec{x}_r \in \mathcal{A}$, for $r = 1, \dots, N_r$, where \mathcal{A} is the array aperture, assumed for convenience to be planar and square, of side a , as shown in Figure 1. The unknown sources are located at points $\vec{y}_s \in \mathcal{D}$, where \mathcal{D} is the imaging region, a bounded set with center at distance L from the array, in the direction orthogonal to the aperture, called the range direction. The coordinates in the plane orthogonal to this direction are called cross-range coordinates. We let \mathcal{D} be a rectangular prism with square cross-section of side D in the cross-range plane, satisfying $L \gg a > D$, and side D_3 in the range direction, satisfying $L \gg D_3$. These scaling relations are typical in most imaging applications.

^{*}L. Borcea is with the Department of Mathematics, University of Michigan, Ann Arbor, MI 48109 USA, e-mail: borcea@umich.edu.

[†]I. Kocyigit is with the Department of Mathematics, Dartmouth College, Hanover, NH 03755 USA, e-mail: ilker.kocyigit@dartmouth.edu

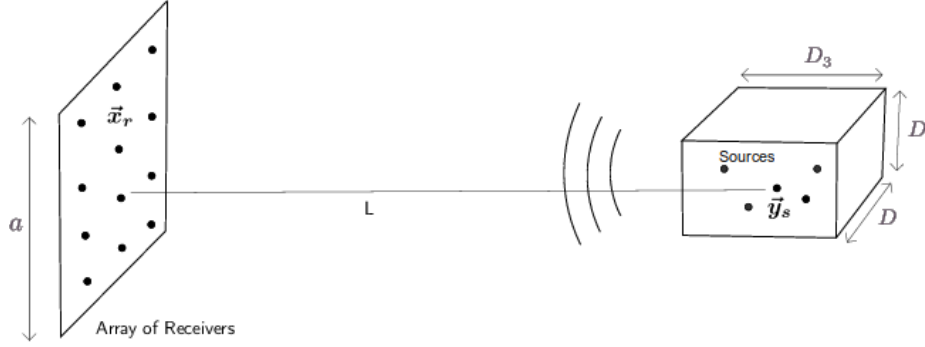


Figure 1: Imaging setup with an array of receivers that is planar square of side a . The range direction is orthogonal to the array aperture. The unknown sources are in the imaging region, a rectangular prism with size D_3 in range and D in cross-range.

The waves are modeled by the pressure $p(t, \vec{x})$, the solution of the equation

$$\frac{1}{c^2(\vec{x})} \partial_t^2 p(t, \vec{x}) - \Delta p(t, \vec{x}) = \sum_{s=1}^{N_s} f_s(t) \delta(\vec{x} - \vec{y}_s), \quad (1)$$

for $\vec{x} \in \mathbb{R}^3$ and $t \in \mathbb{R}$, with zero initial conditions on $p(t, \vec{x})$ and $\partial_t p(t, \vec{x})$ at time t prior to the source excitation. The variable wave speed

$$c(\vec{x}) = c_o \left[1 + \sigma \mu \left(\frac{\vec{x}}{\ell} \right) \right]^{-1/2} \quad (2)$$

models the heterogeneous medium consisting of a homogeneous background with constant wave speed c_o and numerous weak inhomogeneities of size $O(\ell)$, commonly referred to as clutter. Because these inhomogeneities are unknown in imaging, they introduce uncertainty in the wave propagation, modeled in equation (2) by the dimensionless random process μ of dimensionless argument. We assume that μ is stationary, and bounded almost surely. It has zero mean, and autocorrelation

$$\mathcal{R}_\mu(\vec{x} - \vec{x}') = \mathbb{E}[\mu(\vec{x})\mu(\vec{x}')] = \exp \left[-\frac{|\vec{x} - \vec{x}'|^2}{2} \right], \quad (3)$$

where $\mathbb{E}[\cdot]$ denotes expectation with respect to the distribution of μ . The Gaussian expression of \mathcal{R}_μ is chosen for convenience, but the results extend to any integrable autocorrelation function. The scale ℓ is called the correlation length and $\sigma \ll 1$ quantifies the small amplitude of the fluctuations of $c(\vec{x})$.

The imaging problem is to determine the source locations $\{\vec{y}_s\}_{1 \leq s \leq N_s}$ from the measurements $\{p(t, \vec{x}_r)\}_{r=1, \dots, N_r}$.

1.1 Related work

Each inhomogeneity in clutter is a weak scatterer by itself since $\sigma \ll 1$, but cumulative scattering builds up over long ranges. Mathematically, this manifests in the exponential decay of the coherent wave $\mathbb{E}[p(t, \vec{x})]$ and the increase of the fluctuations $p(t, \vec{x}) - \mathbb{E}[p(t, \vec{x})]$. The range scale \mathcal{S} of decay of the coherent wave is the scattering mean free path [19].

When $L < \mathcal{S}$, the cumulative scattering effects are negligible. Much of the imaging literature considers this case, and coherent methods known as reverse time migration [2], matched filtering or backprojection [10, 13] work well. They are based on the data model

$$p(t, \vec{x}_r) = p_o(t, \vec{x}_r) + W(t, \vec{x}_r), \quad r = 1, \dots, N_r, \quad (4)$$

where $p_o(t, \vec{x}_r)$ is the solution of equation (1) with constant wave speed c_o , and $W(t, \vec{x}_r)$ is additive noise with some statistics, assumed uncorrelated over the receivers. In the simplest form, the imaging function is

$$\mathcal{J}(\vec{y}) = \sum_{r=1}^{N_r} p(\tau(\vec{x}_r, \vec{y}), \vec{x}_r), \quad \vec{y} \in \mathcal{D}, \quad (5)$$

where

$$\tau(\vec{x}_r, \vec{y}) = |\vec{x}_r - \vec{y}|/c_o \quad (6)$$

is the travel time from the imaging point \vec{y} to the receiver at \vec{x}_r . The image is robust to additive noise, and it peaks in the vicinity of the source locations, with cross-range resolution $O(\lambda_o L/a)$ and range resolution $O(c_o/B)$, where $\lambda_o = 2\pi c_o/\omega_o$ is the central wavelength of the waves, calculated in terms of the central frequency ω_o , and B is the bandwidth of the source signals. Better resolution can be achieved using convex, sparsity promoting optimization, if the noise is not too strong, and the sources are separated by more than $\lambda_o L/a$ in cross-range and c_o/B in range, see e.g., [12, 8, 6].

The imaging problem is much more difficult when $L \gg \mathcal{S}$, because the array measurements are significantly affected by scattering in clutter and are no longer approximated by the model (4). If the range L is so large that it exceeds the transport mean free path \mathcal{T} , which is the scale that marks the onset of wave diffusion [19], coherent imaging cannot succeed. We assume an intermediate regime $\mathcal{T} > L \gg \mathcal{S}$, where coherent imaging is still possible. Such imaging must involve statistical stabilization with respect to the uncertainty of clutter, so that the estimates of the source locations are insensitive to the particular realization of the random medium (clutter) in which the imaging takes place.

Statistical stability can be obtained with the coherent interferometric (CINT) approach [4, 3], which forms images using the cross-correlations

$$\begin{aligned} \mathcal{C}(t, \tilde{t}, \vec{x}_r, \vec{x}_{r'}) &= \int_{-\infty}^{\infty} ds \Omega \Phi[\Omega(t-s)] \times \\ &\quad p\left(s - \frac{\tilde{t}}{2}, \vec{x}_r\right) p^*\left(s + \frac{\tilde{t}}{2}, \vec{x}_{r'}\right), \end{aligned} \quad (7)$$

where the star denotes complex conjugate. These are calculated around the time t , in a time window modeled by the function Φ of dimensionless argument and $O(1)$ support. The

parameter Ω is adjustable and it should be similar to Ω_d , the frequency offset over which the waves decorrelate in the random medium [19, 4]. Because the waves also decorrelate over directions of arrival, only cross-correlations at nearby receivers are useful. Thus, CINT uses a spatial windowing function Ψ of dimensionless argument and $O(1)$ support to ensure that the receivers in (7) are at distance $|\vec{x}_r - \vec{x}_{r'}| \leq X$, with adjustable parameter that optimally equals the decorrelation length [4]. This scale is proportional to the wavelength, but typically $B \ll \omega_o$, so the decorrelation length X_d is approximately constant in the bandwidth. The CINT imaging function is

$$\mathcal{J}(\vec{y}) = \sum_{r,r'=1}^{N_r} \Psi\left(\frac{|\vec{x}_r - \vec{x}_{r'}|}{X}\right) \times \mathcal{C}(\bar{\tau}(\vec{x}_r, \vec{x}_{r'}, \vec{y}), \tilde{\tau}(\vec{x}_r, \vec{x}_{r'}, \vec{y}), \vec{x}_r, \vec{x}_{r'}), \quad (8)$$

where

$$\begin{aligned} \bar{\tau}(\vec{x}_r, \vec{x}_{r'}, \vec{y}) &= \frac{1}{2} [\tau(\vec{x}_r, \vec{y}) + \tau(\vec{x}_{r'}, \vec{y})], \\ \tilde{\tau}(\vec{x}_r, \vec{x}_{r'}, \vec{y}) &= \tau(\vec{x}_r, \vec{y}) - \tau(\vec{x}_{r'}, \vec{y}). \end{aligned}$$

It is statistically stable with respect to the realizations of the random medium if $\Omega \leq \Omega_d \ll B$ and $X \leq X_d \ll a$, meaning that its expectation near the peaks is much larger than the standard deviation [3]. Moreover, these peaks are in the vicinity of the source locations with resolution $O(\lambda_o L/X)$ in cross-range and $O(c_o/\Omega)$ in range. These resolution limits are similar to those in homogeneous media, except that the aperture size a and bandwidth B are replaced by the windowing parameters X and Ω . These are necessarily smaller than a and B to have statistical stability, so the images are blurrier.

It is shown in [7] that the resolution of CINT images may be improved using convex optimization. However, this requires detailed knowledge of the blurring kernel i.e., prior calibration. The deblurring also works best when the sources are separated by distances larger than $\lambda_o L/X$ in cross-range and c_o/Ω in range, in the sense that if this is not so, there is no guarantee of unique recovery of the source locations.

1.2 Contributions

In this paper we show how, by slightly modifying the CINT imaging function (8), it is possible to recover the unknown sources almost as well as in homogeneous media. Explicitly, we show that a collection of sources that are within a blurred peak of the CINT image and are separated by distances $O(\lambda_o L/a)$ in cross-range and $O(c_o/B)$ in range, can be estimated up to a translation in the support of the CINT peak. We introduce an algorithm that achieves this result, motivate it from first principles and assess its performance with numerical simulations.

Note that although we restrict our study to passive array imaging, the results generalize easily to active arrays that probe the medium with waves and record the echoes, in order to determine point-like scatterers with much larger reflectivity than σ , the reflectivity of the clutter inhomogeneities. These scatterers are secondary sources of waves, which emit signals proportional to the incident wave, so they can be viewed as the unknown sources considered

here. This is obvious in the single scattering (Born) approximation, but it extends to multiple scattering as well, as explained in [9]. Point-like scatterers play an important role in sonar and radar imaging because corners of targets create stronger echoes than other features. Thus, the images are often a constellation of peaks from which target features are to be extracted [14]. Our algorithm can be used for this purpose in random media, because it recovers the relative location of the corner reflectors with the same resolution as in homogeneous media.

The paper is organized as follows: In section 2 we introduce and analyze the CINT-like imaging function. In section 3 we use this function in the source reconstruction algorithm. We illustrate the performance of this algorithm with numerical simulations in section 4, and conclude with a summary in section 5.

2 The CINT-like imaging function

We propose a simple modification of (8), where instead of searching for a single point $\vec{y} \in \mathcal{D}$, we have two search points $\vec{y}, \vec{y}' \in \mathcal{D}$. The CINT-like imaging function

$$\mathcal{I}(\vec{y}, \vec{y}') = \sum_{r, r'=1}^{N_r} \Psi\left(\frac{|\vec{x}_r - \vec{x}_{r'}|}{X}\right) \times \mathcal{C}(\bar{\tau}(\vec{x}_r, \vec{x}_{r'}, \vec{y}, \vec{y}'), \tilde{\tau}(\vec{x}_r, \vec{x}_{r'}, \vec{y}, \vec{y}'), \vec{x}_r, \vec{x}_{r'}), \quad (9)$$

superposes the cross-correlations (7) evaluated at the \vec{y}, \vec{y}' dependent travel times

$$\bar{\tau}(\vec{x}_r, \vec{x}_{r'}, \vec{y}, \vec{y}') = \frac{1}{2} [\tau(\vec{x}_r, \vec{y}) + \tau(\vec{x}_{r'}, \vec{y}')], \quad (10)$$

$$\tilde{\tau}(\vec{x}_r, \vec{x}_{r'}, \vec{y}, \vec{y}') = \tau(\vec{x}_r, \vec{y}) - \tau(\vec{x}_{r'}, \vec{y}'). \quad (11)$$

To explain why this is beneficial, we derive below the expression of $\mathcal{I}(\vec{y}, \vec{y}')$ using a random travel time model [17] that accounts for large, random wavefront distortions in random media, as assumed in adaptive optics [1]. This model is convenient for the calculations and has been used in the analysis of CINT imaging in random media in [3, 7].

As shown in the appendix A, the calculations are based on the expression of the second statistical moments of the pressure waves, which are qualitatively similar to those in stronger scattering regimes [17, 5]. Thus, the results extend verbatim to such regimes.

2.1 Setup and the random travel time model

We introduce here a few assumptions that simplify the calculations and lead to an explicit expression of (9).

The first assumption is that the sources emit the same pulse

$$f_s(t) = f(t) = \left(\frac{2}{\pi}\right)^{1/4} \sqrt{B} \exp[-i\omega_o t - tB^2], \quad (12)$$

modulated at central frequency ω_o , with Gaussian envelope normalized so that $\|f\|_2 = 1$. The Fourier transform of this pulse

$$\hat{f}(\omega) = \left(\frac{\sqrt{2\pi}}{B} \right)^{1/2} \exp \left[-\frac{(\omega - \omega_o)^2}{4B^2} \right], \quad (13)$$

is also a Gaussian, centered at the frequency ω_o and with standard deviation proportional to B , called in an abuse of terminology the bandwidth. We assume that $B \ll \omega_o$. In general, the sources will not emit the same signal and moreover, the signal may not be a pulse. The imaging algorithm in this paper applies to arbitrary $f_s(t)$, that may even be noise-like, as long as for nearby sources these signals are statistically correlated. This holds for example in active array imaging, where unknown scatterers act as secondary sources of waves and $f_s(t)$ are given by the convolution of the probing signal emitted by the array and the Green's function that propagate the waves in the random medium to the scatterer locations.

The second assumption is that at any given frequency ω in the support of (13), the wave propagation can be modeled by the Green's function

$$\hat{G}(\omega, \vec{x}, \vec{y}) = \frac{\exp \{i\omega [\tau(\vec{x}, \vec{y}) + \delta\tau(\vec{x}, \vec{y})]\}}{4\pi|\vec{x} - \vec{y}|} \quad (14)$$

of Helmholtz's equation, where

$$\delta\tau(\vec{x}, \vec{y}) = \frac{\sigma|\vec{x} - \vec{y}|}{2c_o} \int_0^1 du \mu \left(\frac{(1-u)\vec{y} + u\vec{x}}{\ell} \right). \quad (15)$$

This is the random travel time model and we refer to [3, 17] for a detailed discussion of its range of validity. Here it suffices to say that it holds when $\lambda_o \ll \ell \ll a \ll L$ and σ is sufficiently small. We also recall from [3, Lemma 3.1] that the random process (15) is approximately Gaussian, with mean zero and standard deviation $O(\sigma\sqrt{\ell L}/\lambda_o)$.

The third assumption is that the size of the imaging region satisfies the scaling relations

$$\frac{\lambda_o L}{X} \ll D \leq a, \quad \frac{c_o}{\Omega} \ll D_3. \quad (16)$$

The lower bounds in these relations are the CINT resolution limits, so this assumption ensures that the search domain is large enough to observe the focusing of the CINT imaging function (8). We also suppose that the aperture size a and the size of the imaging region are sufficiently small so that the rays connecting the sources and receivers are contained within a narrow cone of small opening angle and axis along the range direction. This assumption is described in more detail in the appendix A and in technical terms it means that the waves are in a paraxial propagation regime.

Finally, to carry out explicit calculations, we take the Gaussian window functions

$$\Phi(\Omega t) = \exp \left[-\frac{(\Omega t)^2}{2} \right], \quad (17)$$

$$\Psi \left(\frac{|\vec{x}_r - \vec{x}_{r'}|}{X} \right) = \exp \left[-\frac{|\vec{x}_r - \vec{x}_{r'}|^2}{2X^2} \right], \quad (18)$$

in definitions (7) and (9). We also suppose that the receivers are spaced at $O(\lambda_o)$ distances, so that $N_r = O(a^2/\lambda_o^2) \gg 1$. This allows us to approximate the sums over the receivers by integrals over the aperture \mathcal{A} . To avoid specifying the aperture size in these integrals, we use the Gaussian apodization

$$\exp \left[-|\vec{x}|^2 / (2(a/6)^2) \right], \quad \vec{x} \in \mathcal{A},$$

which is negligible outside the disk of radius $a/2$.

2.2 The imaging kernel

For simplicity, we neglect additive noise in the calculations in this section, although noise is considered in the numerical simulations in section 4. As shown in the appendix A, in the setup described in section 2.1, the imaging function (9) can be written as

$$\mathcal{I}(\vec{y}, \vec{y}') = \sum_{s,s'=1}^{N_s} \mathcal{K}(\vec{y}, \vec{y}', \vec{y}_s, \vec{y}_{s'}), \quad (19)$$

with kernel \mathcal{K} that depends on the search points \vec{y}, \vec{y}' and the locations \vec{y}_s and $\vec{y}_{s'}$ of pairs of the unknown sources. To describe this kernel, consider the system of coordinates with origin at the center of the array and write $\vec{y} = (\mathbf{y}, y_3)$, with two dimensional vector \mathbf{y} in the cross-range plane and range coordinate y_3 . Define also the center and difference cross-range vectors

$$\bar{\mathbf{y}} = \frac{\mathbf{y} + \mathbf{y}'}{2}, \quad \tilde{\mathbf{y}} = \mathbf{y} - \mathbf{y}', \quad (20)$$

and the center and difference range coordinates

$$\bar{y}_3 = \frac{y_3 + y'_3}{2}, \quad \tilde{y}_3 = y_3 - y'_3. \quad (21)$$

Similarly, we let $\vec{y}_s = (\mathbf{y}_s, y_{s,3})$ and define

$$\bar{\mathbf{y}}_{ss'} = \frac{\mathbf{y}_s + \mathbf{y}_{s'}}{2}, \quad \tilde{\mathbf{y}}_{ss'} = \mathbf{y}_s - \mathbf{y}_{s'}, \quad (22)$$

$$\bar{y}_{ss',3} = \frac{y_{s,3} + y_{s',3}}{2}, \quad \tilde{y}_{ss',3} = y_{s,3} - y_{s',3}, \quad (23)$$

for all $s, s' = 1, \dots, N_s$.

The kernel satisfies

$$|\mathcal{K}(\vec{y}, \vec{y}', \vec{y}_s, \vec{y}_{s'})| \sim \exp \left\{ -\frac{|\tilde{\mathbf{y}}_{ss'}|^2}{2\gamma X_d^2} - \frac{|\tilde{y}_{ss',3} - \tilde{y}_3|^2}{2(c_o/B)^2} - \frac{|\tilde{\mathbf{y}}_{ss'} - \tilde{\mathbf{y}}|^2}{2[\gamma_1 L / (k_o a)]^2} - \frac{|\bar{\mathbf{y}}_{ss'} - \bar{\mathbf{y}}|^2}{2[L / (k_o X_e)]^2} - \frac{(|(\bar{\mathbf{y}}_{ss'}, \bar{y}_{ss',3})| - |(\bar{\mathbf{y}}, \bar{y}_3)|)^2}{2(c_o/\Omega_e)^2} \right\}, \quad (24)$$

where \sim means of the order of, up to a multiplicative constant. We refer to the appendix A for the detailed expression of \mathcal{K} , not just its absolute value. In (24) we introduced the wavenumber

$$k_o = \omega_o/c_o = 2\pi/\lambda_o$$

and the positive coefficients $\gamma, \gamma_1 \geq O(1)$. We also denote by Ω_e and X_e the frequency and length scales defined by

$$\frac{1}{\Omega_e^2} = \frac{1}{\Omega^2} + \frac{1}{\Omega_d^2} + \frac{1}{4B^2}, \quad (25)$$

$$\frac{1}{X_e^2} = \frac{1}{X^2} + \frac{1}{X_d^2} + \frac{1}{4(a/6)^2}. \quad (26)$$

Since $B \gg \Omega_d$ and $a \gg X_d$, the optimal windowing choice $\Omega = O(\Omega_d)$ and $X = O(X_d)$ gives

$$\Omega_e = O(\Omega_d) \ll B, \quad X_e = O(X_d) \ll a. \quad (27)$$

The expression (24) says that the imaging function peaks when the center $\frac{1}{2}(\vec{\mathbf{y}} + \vec{\mathbf{y}}')$ of the imaging points is in the vicinity of $\frac{1}{2}(\vec{\mathbf{y}}_s + \vec{\mathbf{y}}_{s'})$, for some pair s, s' of source indexes. The radius of this vicinity is $O(\lambda_o L/X_e)$ in the cross-range plane and $O(c_o/\Omega_e)$ in the range direction. This is the same as the focusing of the CINT image (8). The new observation is that we can get much better estimates of the source offsets $\vec{\mathbf{y}}_s - \vec{\mathbf{y}}_{s'}$, with the same resolution as in the homogeneous medium i.e., $O(\lambda_o L/a)$ in cross-range and $O(c_o/B)$ in range.

3 The imaging algorithm

The imaging algorithms consists of the following steps:

Step 1: Calculate the CINT image (8), which is the same as $\mathcal{I}(\vec{\mathbf{y}}, \vec{\mathbf{y}})$, and identify its peaks in the search domain \mathcal{D} . The unknown sources lie in the support of these peaks, but they cannot be identified due to the poor resolution: $O(\lambda_o L/X_e)$ in cross-range and $O(c_o/\Omega_e)$ in range. To reduce the computations, it suffices to form the CINT image on a coarse mesh with pixel size similar to these resolution limits.

Step 2: Let $\vec{\mathbf{z}}_o$ be the location of the center of a CINT peak. Suppose that there are $n_s \leq N_s$ sources within this peak and denote by \mathcal{Y} the set of their locations. We can only expect to determine these locations up to an overall translation, so we set $\vec{\mathbf{z}}_o$ as one point in the constellation of n_s sources. To estimate the other locations, relative to $\vec{\mathbf{z}}_o$, calculate $\mathcal{I}(\vec{\mathbf{z}}_o, \vec{\mathbf{y}})$ for $\vec{\mathbf{y}}$ in the support of the CINT peak, on a refined imaging mesh with pixel size $O(\lambda_o L/a)$ in cross-range and $O(c_o/B)$ in range. These are the resolution limits for the source offsets in equation (24).

Step 3: Identify the peaks of $\mathcal{I}(\vec{\mathbf{z}}_o, \vec{\mathbf{y}})$, which are the points $\vec{\mathbf{z}}_j$ satisfying

$$\vec{\mathbf{z}}_j - \vec{\mathbf{z}}_o \in \mathcal{E}(\mathcal{Y}), \quad (28)$$

where

$$\mathcal{E}(\mathcal{Y}) = \{\vec{\mathbf{y}}_s - \vec{\mathbf{y}}_{s'} : \vec{\mathbf{y}}_s, \vec{\mathbf{y}}_{s'} \in \mathcal{Y}, \vec{\mathbf{y}}_s \neq \vec{\mathbf{y}}_{s'}\}. \quad (29)$$

The set $\mathcal{E}(\mathcal{Y})$ has cardinality $n_s(n_s - 1)$ in most cases, where the offset vectors $\vec{y}_s - \vec{y}_{s'}$ are distinct for different pairs (s, s') , with $s, s' = 1, \dots, n_s$ and $s \neq s'$. Thus, $\mathcal{I}(\vec{z}_0, \vec{y})$ is expected to have $N_z = n_s(n_s - 1)$ peaks. This count reflects that if $\vec{e} \in \mathcal{E}(\mathcal{Y})$, then $-\vec{e} \in \mathcal{E}(\mathcal{Y})$, as well. However, there are special, unlikely cases, where different source pairs give the same offset vectors. Thus, in general,

$$N_z \leq n_s(n_s - 1).$$

Step 4: From the N_z peaks of $\mathcal{I}(\vec{z}_0, \vec{y})$ estimate the set (29) by

$$\mathcal{E}^{\text{est}} = \{\vec{z}_j - \vec{z}_o, \quad j = 1, \dots, N_z\}. \quad (30)$$

Use this set to determine the constellation of sources. For our purpose, it suffices to use the exhaustive search algorithm given below, which is not optimal in terms of computational cost. The output of this algorithm is a set \mathcal{Y}^{est} of points \vec{y}_s^{est} , so that

$$\mathcal{E}(\mathcal{Y}^{\text{est}}) = \mathcal{E}^{\text{est}}. \quad (31)$$

Here $\mathcal{E}(\mathcal{Y}^{\text{est}})$ is defined as in (29), with \mathcal{Y} replaced by \mathcal{Y}^{est} . The vectors in \mathcal{Y}^{est} are the estimates of the source locations, up to the translation defined by fixing one source at \vec{z}_o and the reflection about \vec{z}_o .

Algorithm(E, Y)

Input: The sets E , and Y .

Output: Empty set or a non-empty set \mathcal{Y}^{est} .

1. **If** $\mathcal{E}(Y) = \mathcal{E}^{\text{est}}$ **then**
2. return $\mathcal{Y}^{\text{est}} = Y$
3. **End-If**
4. **While** $E \neq \emptyset$ **do**
5. Select the first vector \vec{e} and set $E = E \setminus \{\vec{e}\}$
6. **Let** $\vec{y} = \vec{z}_o + \vec{e}$
7. **If** $\{\pm(Y - \vec{y})\} \subset \mathcal{E}^{\text{est}}$ **then**
8. $Y' = \text{Algorithm}(E, Y \cup \{\vec{y}\})$
9. **If** $Y' \neq \emptyset$ **then**
10. return $\mathcal{Y}^{\text{est}} = Y'$
11. **End-If**
12. **End-If**
13. **End-While**
14. return \emptyset

3.1 Discussion

The first call of this recursive algorithm is made with the inputs $E = \mathcal{E}^{\text{est}}$ and $Y = \{\vec{z}_o\}$. When the algorithm outputs the empty set \emptyset , the search has failed. We show in the appendix B that, when noise is not an issue i.e., the offset vectors in the set \mathcal{E}^{est} are the same as those in $\mathcal{E}(\mathcal{Y})$, the output of the algorithm is necessarily a non empty set \mathcal{Y}^{est} satisfying (31). In practice, the testing of the equalities and the inclusion at lines 1 and 7 can be done up to

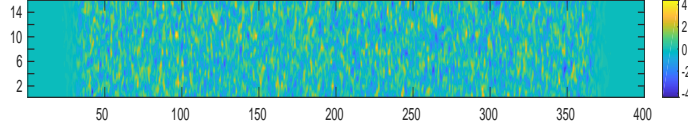


Figure 2: Display of the realization of the fluctuations μ used in the numerical results. The abscissa is range in units of ℓ and the ordinate is cross-range in units of ℓ .

some tolerance. In our numerical simulations we consider two vectors to be same if their difference has cross-range and range components that are smaller than the pixel size, in absolute value.

Note that the expression (24) of the imaging kernel indicates that only sources at cross-range offsets $|\mathbf{y}_s - \mathbf{y}'_s| \leq O(\sqrt{\gamma}X_d)$ contribute to the image $\mathcal{I}(\mathbf{z}_0, \mathbf{y})$ calculated at step 2. This distance is at least $O(\lambda_o L/X_e)$ in our case, so all the sources supported in the CINT peak should contribute to $\mathcal{I}(\mathbf{z}_0, \mathbf{y})$. In other scattering regimes it may be that $X_d \ll \lambda_o L/X_e$, so the support of the CINT peak may be divided in smaller sets at step 2. The remainder of the algorithm above can be used separately for each such set.

We already stated that we can only hope to determine the set \mathcal{Y} of source locations up to an overall translation, fixed by the starting point \mathbf{z}_o and up to a reflection. This is due to the fact that the set \mathcal{Y}^{ref} , defined as the reflection of \mathcal{Y} with respect to a fixed point, satisfies $\mathcal{E}(\mathcal{Y}) = \mathcal{E}(\mathcal{Y}^{\text{ref}})$.

3.2 Relation to localization

The estimation of the source locations from the set \mathcal{E}^{est} of offset vectors is somewhat related to the network localization problem [20], [21]: Let $\mathcal{N} = \{\mathbf{n}_1, \mathbf{n}_2, \dots, \mathbf{n}_m\}$ denote the unknown set of nodes of a network. Determine \mathcal{N} from knowledge of a non-empty subset $\mathcal{B} \subset \mathcal{N}$ of so-called beacon nodes and the distance map $\delta : \mathcal{N} \times \mathcal{N} \rightarrow \mathbb{R}^+$, defined by $\delta(i, j) = \|\mathbf{n}_i - \mathbf{n}_j\|$, for $i, j = 1, \dots, m$.

Our problem is different as follows: (1) The data are the offset vectors $\vec{\mathbf{y}}_j - \vec{\mathbf{y}}_{j'}$ and not just their norm. (2) We do not have access to the distance map δ , we only know its image. That is to say, for any offset vector $\vec{\mathbf{e}} \in \mathcal{E}^{\text{est}}$, we do not know the pair (i, j) of sources that give $\vec{\mathbf{y}}_i - \vec{\mathbf{y}}_j = \vec{\mathbf{e}}$. (3) As explained at Step 3 in section 3, in general, we do not know the number of sources. Only under the additional assumption that there is a unique pair of sources that gives an offset vector $\vec{\mathbf{e}} \in \mathcal{E}^{\text{est}}$, we can determine the number of sources from the cardinality of the set \mathcal{E}^{est} .

4 Numerical results

To minimize the computational cost, we present imaging results in two dimensions, in the plane define by the range axis and one cross-range direction. The array cross-section in this plane is the line segment $[-a/2, a/2]$.

4.1 Simulations setup

The data are obtained using the model

$$p(t, \vec{x}_r) = \int_{-\infty}^{\infty} \frac{d\omega}{2\pi} e^{-i\omega t} \left[\widehat{p}(\omega, \vec{x}_r) + \widehat{W}(\omega, \vec{x}_r) \right], \quad (32)$$

where \widehat{W} denotes additive noise and

$$\widehat{p}(\omega, \vec{x}_r) = \widehat{f}(\omega) \sum_{s=1}^{N_s} \widehat{G}(\omega, \vec{x}_r, \vec{y}_s) \quad (33)$$

is the solution of Helmholtz's equation in the cluttered medium. The noise \widehat{W} is complex Gaussian, uncorrelated over the receivers and frequencies, with mean zero and standard deviation 5% of the maximum absolute value of (33). The Green's function \widehat{G} is calculated using definitions (14)-(15), in the realization of the random medium displayed in Figure 2. This realization is generated using random Fourier series [11], for the autocorrelation (3).

All the length scales are relative to the correlation length ℓ . The central wavelength is $\lambda_o = 1.1 \cdot 10^{-5} \ell$, the array aperture size is $a = 16\ell$ and the range scale is $L = 800\ell$. The frequencies are scaled with respect to ω_o and the bandwidth is $B = \omega_o/5$. The strength of the fluctuations is $\sigma = 2 \cdot 10^{-6}$ and the decorrelation frequency and length defined in (43) are $\Omega_d = 0.039\omega_o$ and $X_d = 0.068\ell$. The window parameters are $X = X_d/3$ and $\Omega = \Omega_d/3$, so definitions (25)–(26) give $X_e = 0.0214\ell$ and $\Omega_e = 0.0124\omega_o$ and the decay scales in the expression of the kernel are

$$\begin{aligned} \frac{L}{k_o X_e} &= 0.0654\ell, & \frac{c_o}{\Omega_e} &= 1.4 \cdot 10^{-4}\ell, \\ \frac{L}{k_o a} &= 8.8 \cdot 10^{-5}\ell, & \frac{c_o}{B} &= 8.8 \cdot 10^{-6}\ell. \end{aligned}$$

The coefficient γ in (24) is

$$\gamma = \frac{4X_d^2}{4X_d^2 - X_e^2} = 1.025$$

and $\gamma_1 \geq 6\sqrt{2}$.

The images displayed in the next section are calculated on an imaging mesh with pixel size $3.92L/(k_o a)$ in cross-range and $0.537c_o/B$ in range. The axes in the plots are in units of the CINT resolution limits.

4.2 Source reconstructions

We present in Figure 3 the results for three nearby sources. As expected, the CINT image $\mathcal{I}(\vec{y}, \vec{y})$ displayed in the top left plot has a blurry peak, and cannot distinguish the sources. The conventional image displayed in the top right plot is calculated using definition (5). It has many spurious peaks and our simulations show that these peaks change unpredictably from one realization of the random process μ to another. This statistical instability is expected, because the data are incoherent in our regime.

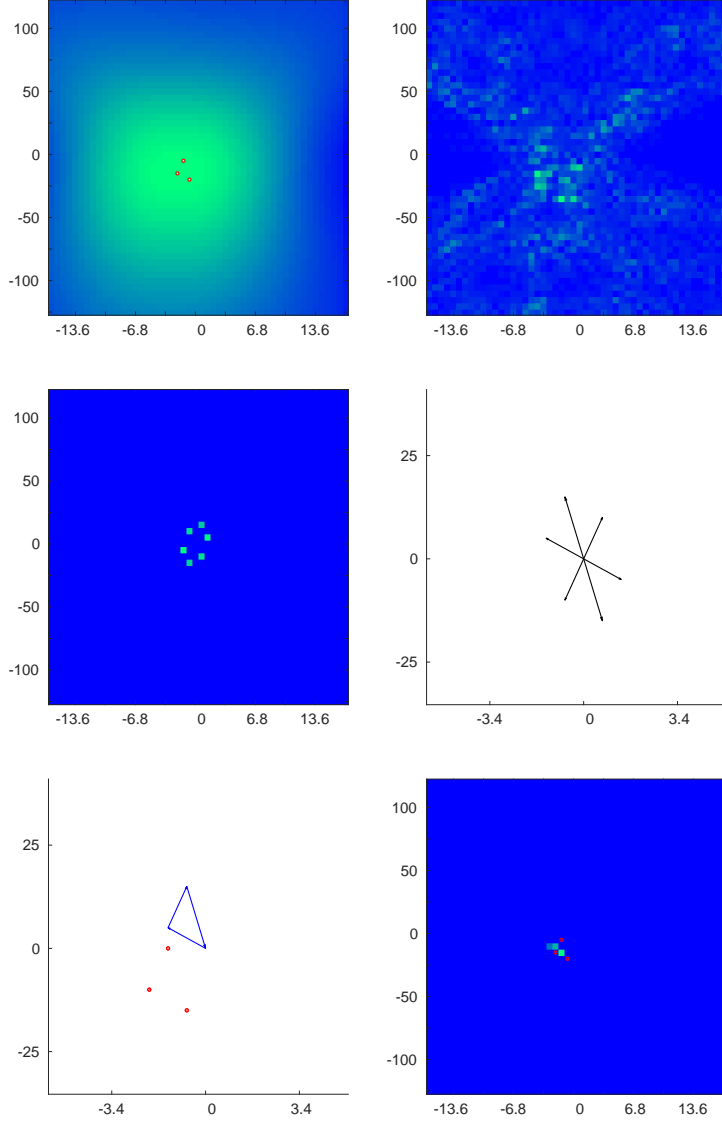


Figure 3: Top row: CINT image $\mathcal{I}(\vec{y}, \vec{y})$ of three sources shown in red (left plot) and the conventional image (5) (right plot). Middle row: The image $\mathcal{I}(\vec{z}_o, \vec{y})$ (left plot) and the offset vectors that define the set (30) (right plot). Bottom row: Reconstruction of the three sources (left plot) and reconstruction by deblurring the CINT image using convex optimization (right plot). The abscissa is range offset with respect to the center location \vec{z}_o of the CINT peak, in units of $L/(k_o a)$. The ordinate is cross-range offset with respect to \vec{z}_o , in units of c_o/B .

In the left plot of the middle row we display the image $\mathcal{I}(\vec{z}_o, \vec{y})$, with \vec{z}_o at the center of the CINT peak. Because we have $n_s = 3$ sources supported in this peak, we observe $N_z = 6$ peaks \vec{z}_j , for $j = 1, \dots, 6$. These define the set \mathcal{E}^{est} defined in (30), with offset vectors displayed in the right plot of the middle row. Note that for each vector \vec{e} in \mathcal{E}^{est} we also have the vector $-\vec{e}$. The reconstruction of the sources using the algorithm described in section 3 is

shown in the bottom left plot. The reconstruction is exact up to the translation by the vector \vec{z}_o , where by exact we mean with error that is smaller than the pixel size. For comparison, we also show in the bottom right plot the reconstruction obtained with the deblurring algorithm introduced in [7]. This algorithm is guaranteed to give a good reconstruction of the sources when they are further apart than the CINT resolution limits. In this simulation the sources are much closer to each other so the results are worse than those in the bottom left plot. As predicted by the theory in [7], the reconstruction in the bottom right plot is peaked near the source locations, but it does not show three distinct sources.

In Figure 4 we show the reconstruction of 4 sources. As in the previous example, the sources are located in the support of the CINT peak. The image $\mathcal{I}(\vec{z}_o, \vec{y})$ shown in the top right plot has one spurious peak, due to the noise. However, this can be easily filtered out because the offset vector $\vec{e} \in \mathcal{E}^{\text{est}}$ corresponding to it does not have the property that $-\vec{e} \in \mathcal{E}^{\text{est}}$. The set of remaining offset vectors is displayed in the left bottom plot and the reconstruction of the four sources is shown in the bottom right plot. The reconstruction is exact, up to the translation by \vec{z}_o .

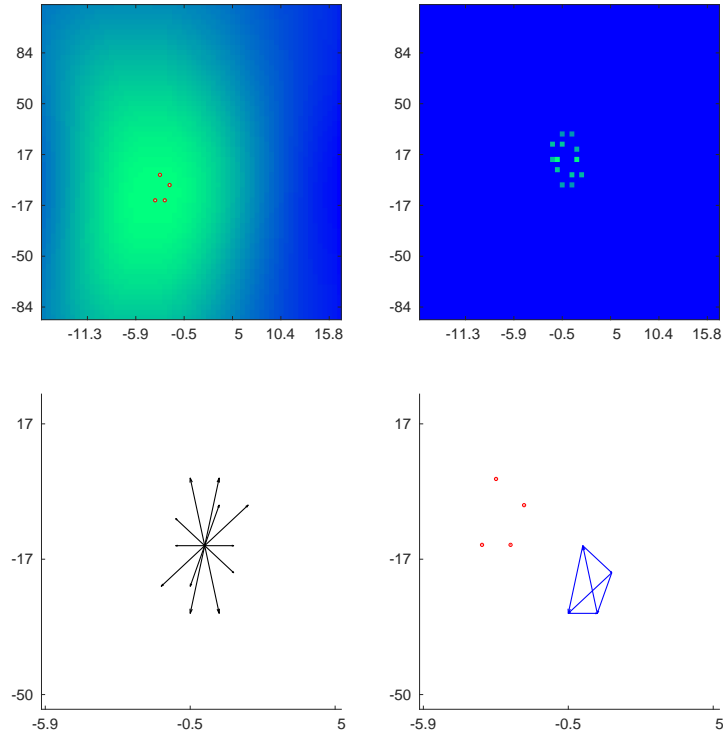


Figure 4: Top row: Left: CINT image $\mathcal{I}(\vec{y}, \vec{y})$ of four sources shown in red. Right: The image $\mathcal{I}(\vec{z}_o, \vec{y})$. Bottom row: Left: The offset vectors that define the set (30). Right: Reconstruction of the four sources. The axes are as in Figure 3.

5 Summary

We introduced a novel algorithm for array imaging in cluttered media modeled by a random sound speed. The algorithm is designed to work in the presence of strong scattering effects in clutter, where the sound waves recorded at the array are incoherent i.e., their statistical expectation is close to zero. Physically, this means that the range offset between the unknown sources and the array is larger than the scattering mean free path in clutter. The algorithm uses an imaging approach that is similar to the coherent interferometric (CINT) method. CINT is known to be robust to clutter scattering effects, as long as the waves are not in a diffusion regime i.e., for ranges less than a transport mean free path. The robustness comes at the cost of image blur. This impedes imaging of sources at nearby locations \vec{y}_s , for $s = 1, \dots, N_s$. The algorithm introduced in this paper uses the observation that the blur affects only the estimation of the center locations $(\vec{y}_s + \vec{y}_{s'})/2$ of pairs (s, s') of sources, whereas the offset vectors $\vec{y}_s - \vec{y}_{s'}$ can be estimated with the same resolution as in the absence of clutter. Thus, it is possible to determine constellations of nearby sources, up to a translation within the support of a peak of the CINT image.

We motivated the algorithm from first principles, starting with the wave equation in random media and assessed its performance with numerical simulations. To simplify the presentation, we considered a high frequency scattering regime defined by large, random wavefront distortions of the waves received at the array, although as explained in the paper, the results extend verbatim to stronger scattering regimes.

Appendix A

In this appendix we derive the expression (24). We begin with the solution of the wave equation (1) evaluated at the receiver location $\vec{x}_r = (\mathbf{x}_r, 0)$,

$$p(t, \vec{x}_r) = \int_{-\infty}^{\infty} \frac{d\omega}{2\pi} e^{-i\omega t} \hat{f}(\omega) \sum_{s=1}^{N_s} \hat{G}(\omega, \vec{x}_r, \vec{y}_s), \quad (34)$$

where we used the assumption (12) and \hat{G} is the Green's function modeled by (14). This model holds under the assumptions

$$\ell \gg \sqrt{\lambda_o L} \gg \lambda_o, \quad \sigma \ll \frac{\sqrt{\lambda_o \ell}}{L}, \quad (35)$$

as explained in [17, 3, 7]. These ensure that the waves propagate along straight rays, as in geometrical optics, and that the random fluctuations of the amplitude of the Green's function are negligible. The first bound on ℓ is to have consistent assumptions on σ ,

$$\frac{\lambda_o}{\sqrt{\ell L}} \ll \frac{\lambda_o^{2/3} \ell^{1/6}}{L^{5/6}} \ll \sigma \ll \frac{\sqrt{\lambda_o \ell}}{L}, \quad (36)$$

chosen large enough to give large random travel time fluctuations, as explained in section 2.1.

It is shown in [7, Proposition 3.1] that the expectation of the Green's function is

$$\mathbb{E} \left[\widehat{G}(\omega, \vec{x}_r, \vec{y}_s) \right] \approx \frac{e^{i\omega\tau(\vec{x}_r, \vec{y}_s)}}{4\pi|\vec{x}_r - \vec{y}_s|} e^{-\frac{|\vec{x}_r - \vec{y}_s|}{S}}. \quad (37)$$

The decaying exponential is due to the random phase, which is approximately Gaussian, and the scattering mean free path is defined by

$$S = \frac{8\lambda_o^2}{(2\pi)^{5/2}\sigma^2\ell}. \quad (38)$$

The lower bound on σ in (35) implies that

$$S \ll L = O(|\vec{x}_r - \vec{y}_s|), \quad (39)$$

so the wave recorded at the array is incoherent i.e.,

$$\mathbb{E}[p(t, \vec{x}_r)] \approx 0. \quad (40)$$

The kernel of the imaging function (9) is obtained from equations (7), (19) and (34),

$$\begin{aligned} \mathcal{K}(\vec{y}, \vec{y}', \vec{z}, \vec{z}') &= \sum_{r, r'=1}^{N_r} \Psi\left(\frac{|\vec{x}_r - \vec{x}_{r'}|}{X}\right) \int_{-\infty}^{\infty} \frac{d\omega}{2\pi} \times \\ &\int_{-\infty}^{\infty} \frac{d\tilde{\omega}}{2\pi} \widehat{\Phi}\left(\frac{\tilde{\omega}}{\Omega}\right) \widehat{f}\left(\omega + \frac{\tilde{\omega}}{2}\right) \widehat{f}^{\star}\left(\omega - \frac{\tilde{\omega}}{2}\right) \widehat{G}(\omega, \vec{x}_r, \vec{z}) \times \\ &\widehat{G}^{\star}(\omega, \vec{x}_{r'}, \vec{z}') e^{-i\left(\omega + \frac{\tilde{\omega}}{2}\right)\tau(\vec{x}_r, \vec{y}) + i\left(\omega - \frac{\tilde{\omega}}{2}\right)\tau(\vec{x}_{r'}, \vec{y}')}, \end{aligned} \quad (41)$$

where we replaced \vec{y}_s by \vec{z} and $\vec{y}_{s'}$ by \vec{z}' , to avoid carrying over the source indexes. We use the definitions of \widehat{f} , Ψ and $\widehat{\Phi}$ given in section 2.1, and replace the sum over the receivers by the integral over the aperture, with Gaussian apodization,

$$\sum_{r=1}^{N_r} \rightsquigarrow \frac{N_r}{a^2} \int_{\mathbb{R}^2} d\vec{x} e^{-\frac{|\vec{x}|^2}{2(a/6)^2}}.$$

A.1 Wave decorrelation and the paraxial approximation

Essentially the same calculation as in [3, Section 4] shows that the kernel is statistically stable i.e., it is approximated by its expectation, when

$$X = O(X_d) \ll a.$$

The random travel time model accounts only for wavefront distortion and does not take into consideration delay spread due to scattering. Thus, the bandwidth does not play a big role in the statistical stability. However, in stronger scattering regimes the bandwidth is very important [5] and statistical stability is achieved if

$$\Omega = O(\Omega_d) \ll B,$$

as we assume here.

The second moment formula is derived in [7, Appendix B]

$$\begin{aligned} & \mathbb{E} \left[\widehat{G} \left(\omega + \frac{\tilde{\omega}}{2}, \vec{x}, \vec{z} \right) \widehat{G}^* \left(\omega - \frac{\tilde{\omega}}{2}, \vec{x}', \vec{z}' \right) \right] \\ & \approx \frac{e^{i\omega\tilde{\tau}(\vec{x}, \vec{x}', \vec{z}, \vec{z}') + i\tilde{\omega}\bar{\tau}(\vec{x}, \vec{x}', \vec{z}, \vec{z}')}}{(4\pi)^2 |\vec{x} - \vec{z}| |\vec{x}' - \vec{z}'|} e^{-\frac{1}{S} \|\vec{x} - \vec{z}\| - \|\vec{x}' - \vec{z}'\|} \times \\ & e^{-\frac{1}{2X_d^2} (|\vec{z}' - \vec{z}|^2 + (\vec{z}' - \vec{z}) \cdot (\vec{x}' - \vec{x}) + |\vec{x}' - \vec{x}|^2) - \frac{\tilde{\omega}^2}{2\Omega_d^2}}, \end{aligned} \quad (42)$$

with $\bar{\tau}$ and $\tilde{\tau}$ defined in (10)–(11). It decays with the frequency and cross-range offsets, due to the decorrelation of the waves in the random medium. The decorrelation frequency and length are

$$\Omega_d = \frac{2\omega_o}{(2\pi)^{5/4}} \left(\frac{\lambda_o}{\sigma\sqrt{\ell L}} \right) \ll \omega_o, \quad X_d = \sqrt{3}\ell \frac{\Omega_d}{\omega_o} \ll \ell, \quad (43)$$

where the inequalities are implied by (35).

As stated in section 2.1, we consider a paraxial wave propagation regime, where

$$\omega_o \tau(\vec{x}, \vec{z}) = k_o |\vec{x} - \vec{z}| \approx k_o \left(z_3 + \frac{|\vec{x} - \vec{z}|^2}{2L} \right), \quad (44)$$

with negligible residual

$$O\left(\frac{a^4}{\lambda_o L^3}\right) + O\left(\frac{a^2 D_3}{\lambda_o L^2}\right) \ll 1. \quad (45)$$

Here we used the scaling relation (16). We also approximate the amplitude of the Green's functions by

$$\frac{1}{4\pi |\vec{x} - \vec{z}|} \approx \frac{1}{4\pi L}. \quad (46)$$

Since the expression (42) is large when the cross-range offsets are $O(X_d)$, we estimate from (38), (35) and (45) that

$$\frac{\|\vec{x} - \vec{z}\| - \|\vec{x}' - \vec{z}'\|}{S} \ll 1, \quad (47)$$

so the decaying exponential in the second line of (42) is approximately equal to 1.

A.2 Calculation of the imaging kernel

Because of the decorrelation of the waves over the scale X_d , it suffices to consider imaging points at cross-range offsets $|\mathbf{y} - \mathbf{y}'| \leq O(X_d)$. Substituting the results in (41), and using Ω_e

and X_e defined in (25)–(26), which are similar to Ω_d and X_d , we obtain that

$$\begin{aligned} \mathcal{K}(\vec{y}, \vec{y}', \vec{z}, \vec{z}') &\approx \frac{N_r^2}{2\pi(4\pi L)^2 B a^4} e^{-\frac{|\vec{z}|^2}{2X_d^2}} \times \\ &\int_{\mathbb{R}^2} d\mathbf{x} e^{-\frac{|\mathbf{x}|^2}{(a/6)^2}} \int_{\mathbb{R}^2} d\tilde{\mathbf{x}} e^{-\frac{|\tilde{\mathbf{x}}|^2}{2X_e^2} - \frac{\tilde{\mathbf{x}} \cdot \vec{z}}{2X_d^2}} \times \\ &\int_{-\infty}^{\infty} d\omega e^{-\frac{(\omega - \omega_o)^2}{2B^2} + i\frac{\omega}{c_o} \left[\tilde{z}_3 - \tilde{y}_3 - \frac{\mathbf{x} \cdot (\vec{z} - \tilde{\mathbf{y}})}{L} - \frac{\tilde{\mathbf{x}} \cdot (\vec{z} - \tilde{\mathbf{y}})}{L} + \frac{\vec{z} \cdot \vec{z} - \tilde{\mathbf{y}} \cdot \tilde{\mathbf{y}}}{L} \right]} \times \\ &\int_{-\infty}^{\infty} d\tilde{\omega} e^{-\frac{\tilde{\omega}^2}{2\Omega_e^2} + i\frac{\tilde{\omega}}{c_o} \left[\tilde{z}_3 - \tilde{y}_3 - \frac{\mathbf{x} \cdot (\vec{z} - \tilde{\mathbf{y}})}{L} + \frac{|\vec{z}|^2 - |\tilde{\mathbf{y}}|^2}{2L} \right]}, \end{aligned} \quad (48)$$

with center vectors (\vec{y}, \vec{y}_3) and difference vectors $(\tilde{\mathbf{y}}, \tilde{y}_3)$ defined in (20)–(21). The vectors (\vec{z}, \vec{z}_3) and $(\tilde{\mathbf{z}}, \tilde{z}_3)$ are defined the same way, by replacing \vec{y} and \vec{y}' with \vec{z} and \vec{z}' in (20)–(21). Note that in (48) we neglect the phase terms

$$\frac{\tilde{\omega}}{c_o} \left(\frac{|\tilde{\mathbf{z}}|^2 - |\tilde{\mathbf{y}}|^2}{4L} \right) = O\left(\frac{\Omega_e X_d^2}{c_o L}\right) \ll 1$$

and

$$\frac{\tilde{\omega}}{c_o} \frac{\tilde{\mathbf{x}} \cdot (\tilde{\mathbf{z}} - \tilde{\mathbf{y}})}{L} = O\left(\frac{\Omega_e X_d^2}{c_o L}\right) \ll 1,$$

with the inequalities implied by (27), (35) and (43).

Carrying out the Gaussian integrals in (48), we obtain

$$\begin{aligned} \mathcal{K}(\vec{y}, \vec{y}', \vec{z}, \vec{z}') &\approx H \exp \left\{ -\frac{|\vec{z}|^2}{2\gamma X_d^2} - \frac{\beta^2}{2(1 + \frac{|\vec{\zeta}|^2}{2\theta^2})} \right. \\ &\quad \left. - \frac{v^2 + \eta^2 + 2i\eta v^2 B/\omega_o}{2(1 + \frac{v^2 B^2}{\omega_o^2})} + i\frac{\omega_o \eta}{B} \right\}, \end{aligned} \quad (49)$$

where the amplitude factor is

$$H = \frac{N_r^2 X_e^2 \Omega_e}{288 a^2 L^2 \left(1 + \frac{|\vec{\zeta}|^2}{2\theta^2}\right)^{1/2} \left(1 + \frac{v^2 B^2}{\omega_o^2}\right)^{1/2}},$$

and we used the positive constants θ and γ defined by

$$\theta = \frac{\omega_o X_e}{\Omega_e (a/6)}, \quad \frac{1}{\gamma} = 1 - \frac{X_e^2}{4X_d^2} > \frac{3}{4}.$$

The inequality on γ is implied by definition (26). We also introduced the notation

$$\begin{aligned} \bar{\zeta} &= \frac{\vec{z} - \vec{y}}{L/(k_o X_e)}, \quad \tilde{\zeta} = \frac{\tilde{\mathbf{z}} - \tilde{\mathbf{y}}}{6\sqrt{2}L/(k_o a)}, \\ \beta &= \frac{\tilde{z}_3 - \tilde{y}_3 + \frac{|\vec{z}|^2 - |\tilde{\mathbf{y}}|^2}{2L}}{c_o/\Omega_e} \approx \frac{|(\vec{z}, \vec{z}_3)| - |(\vec{y}, \vec{y}_3)|}{c_o/\Omega_e}, \\ v^2 &= |\bar{\zeta}|^2 + \frac{|\tilde{\zeta}|^2}{1 + \frac{|\tilde{\zeta}|^2}{2\theta^2}} + \frac{|\bar{\zeta}|^2 |\tilde{\zeta}|^2 - |\bar{\zeta} \cdot \tilde{\zeta}|^2}{2\theta^2 \left(1 + \frac{|\tilde{\zeta}|^2}{2\theta^2}\right)}, \end{aligned}$$

and

$$\eta = \frac{B}{c_o} \left[\tilde{z}_3 - \tilde{y}_3 + \frac{\bar{\mathbf{z}} \cdot \tilde{\mathbf{z}} - \bar{\mathbf{y}} \cdot \tilde{\mathbf{y}}}{L} + \frac{X_e^2}{2X_d^2} \frac{\tilde{\mathbf{z}} \cdot (\bar{\mathbf{z}} - \bar{\mathbf{y}})}{L} - \frac{\beta \bar{\boldsymbol{\zeta}} \cdot \tilde{\boldsymbol{\zeta}}}{\sqrt{2}k_o\theta(1 + \frac{|\bar{\boldsymbol{\zeta}}|^2}{2\theta^2})} \right].$$

The expression (49) simplifies, because it is large only when $|v|, |\beta|, |\eta| = O(1)$. Since $B \ll \omega_o$, we can write

$$1 + \frac{v^2 B^2}{\omega_o^2} \approx 1,$$

and neglect the $\eta v^2 B / \omega_o$ phase, with absolute value much less than 1. We also have that $|\bar{\boldsymbol{\zeta}}|$ and $|\tilde{\boldsymbol{\zeta}}|$ are $O(1)$, because $v = O(1)$, and therefore

$$\begin{aligned} \frac{B}{c_o} \left| \frac{\bar{\mathbf{z}} \cdot \tilde{\mathbf{z}} - \bar{\mathbf{y}} \cdot \tilde{\mathbf{y}}}{L} \right| &= \frac{B}{c_o} \left| \frac{\bar{\mathbf{z}} \cdot (\tilde{\mathbf{z}} - \tilde{\mathbf{y}}) + \tilde{\mathbf{y}} \cdot (\bar{\mathbf{z}} - \bar{\mathbf{y}})}{L} \right| \\ &= \frac{B}{\omega_o} \left[O\left(\frac{Dk_o|\tilde{\mathbf{z}} - \tilde{\mathbf{y}}|}{L}\right) + O\left(\frac{Xk_o|\bar{\mathbf{z}} - \bar{\mathbf{y}}|}{L}\right) \right] \\ &= \frac{B}{\omega_o} \left[O\left(\frac{D}{a}\right) + O\left(\frac{X}{X_e}\right) \right] \ll 1. \end{aligned}$$

Similarly, we obtain that

$$\frac{B}{c_o} \left| \frac{X_e^2}{2X_d^2} \frac{\tilde{\mathbf{z}} \cdot (\bar{\mathbf{z}} - \bar{\mathbf{y}})}{L} \right| \ll 1,$$

and

$$\frac{B}{c_o} \left| \frac{\beta \bar{\boldsymbol{\zeta}} \cdot \tilde{\boldsymbol{\zeta}}}{k_o\theta(1 + \frac{|\bar{\boldsymbol{\zeta}}|^2}{2\theta^2})} \right| = O\left(\frac{B}{\omega_o\theta}\right).$$

The definitions of θ , X_e and Ω_e give

$$\theta = O\left(\frac{\ell}{a}\right) \ll 1.$$

We assume that this number is not too small, so that $B/(\omega_o\theta) \ll 1$, and we can use the results above to approximate

$$\eta \approx \frac{B}{c_o} (\tilde{z}_3 - \tilde{y}_3).$$

We can now rewrite the kernel (49) as

$$\begin{aligned} \mathcal{K}(\bar{\mathbf{y}}, \bar{\mathbf{y}}', \bar{\mathbf{z}}, \bar{\mathbf{z}}') &\approx H \exp \left\{ i \frac{\omega_o \eta}{B} - \frac{|\tilde{\mathbf{z}}|^2}{2\gamma X_d^2} - \frac{(\tilde{z}_3 - \tilde{y}_3)^2}{2(c_o/B)^2} \right. \\ &\quad \left. - \frac{||(\bar{\mathbf{z}}, \bar{z}_3)| - |(\bar{\mathbf{y}}, \bar{y}_3)||^2}{2(c_o/\Omega_e)^2(1 + \frac{|\bar{\boldsymbol{\zeta}}|^2}{2\theta^2})} - \frac{v^2}{2} \right\}. \end{aligned} \tag{50}$$

Taking absolute value and using that

$$v^2 \geq |\bar{\zeta}|^2 + \frac{|\tilde{\zeta}|^2}{1 + \frac{|\bar{\zeta}|^2}{2\theta^2}},$$

we obtain the result (24) with $\gamma_1 = 6\sqrt{2\left(1 + \frac{|\bar{\zeta}|^2}{2\theta^2}\right)} \geq O(1)$.

Appendix B

Suppose that there exists a constellation \mathcal{Y}_0 of sources such that $\mathcal{E}^{est} = \mathcal{E}(\mathcal{Y}_0)$. We show here that

$$\mathcal{Y}^{est} = \mathbf{Algorithm}(\mathcal{E}^{est}, \{\vec{z}_0\}) \quad (51)$$

returns a set \mathcal{Y}^{est} such that

$$\mathcal{E}(\mathcal{Y}^{est}) = \mathcal{E}^{est}. \quad (52)$$

Once we show that $\mathcal{Y}^{est} \neq \emptyset$, it is straightforward to see from the definition of **Algorithm** that (52) must holds. It remains to show that \mathcal{Y}^{est} is not an empty set.

For a proof by contradiction, suppose that (51) returns $\mathcal{Y}^{est} = \emptyset$. This means explicitly that each call of **Algorithm** results in executing line 14. Since the set $\mathcal{E}(\mathcal{Y})$ of offsets is translation invariant, let us replace the set $\mathcal{Y} = \{\vec{y}_1, \dots, \vec{y}_{n_s}\}$ of source locations by the set $\mathcal{Y}_o = \{\vec{z}_0, \vec{z}_1, \vec{z}_2, \dots, \vec{z}_{n_s-1}\}$ of translated source locations, with translation defined by \vec{z}_o . Define the vectors

$$\vec{e}_{j_k} = \vec{z}_k - \vec{z}_0, \quad k = 1, \dots, m, \quad m = n_s - 1, \quad (53)$$

which belong to \mathcal{E}^{est} . Note that \mathcal{E}^{est} contains other offset vectors, as well. Without loss of generality, we can assume that the vectors (53) are enumerated in order in \mathcal{E}^{est} , meaning that \vec{e}_{j_k} comes before $\vec{e}_{j_{k+1}}$ for $k \in \{1, \dots, m-1\}$.

1st-Recursion: In the first call of **Algorithm**, the arguments are $E = \mathcal{E}^{est}$ and $Y = \{\vec{z}_0\}$.

Since we assume (51) returned \emptyset , the line 14 was executed. Thus in the while loop, each element of E is selected at line 5. In particular, at line 5, the vector $\vec{e} = \vec{e}_{j_1}$ is removed from the set E , and at line 6 we have

$$\vec{y} = \vec{z}_0 + \vec{e} = \vec{z}_0 + \vec{e}_{j_1} = \vec{z}_1.$$

But then

$$\{\pm(\{\vec{z}_0\} - \vec{y})\} = \{\pm\vec{e}_{j_1}\} \subseteq \mathcal{E}^{est}.$$

Therefore line 8 has to be executed. This will take us to the next recursion.

2nd-Recursion: At this recursion level, E contains the offset vectors $\vec{e}_{j_2}, \dots, \vec{e}_{j_m}$, and $Y = \{\vec{z}_0, \vec{z}_1\}$. We note that $Y \subset \mathcal{Y}_0$ at every recursion level.

Once again, by assumption, line 14 was executed. Therefore, at some iteration of the while loop, at line 5, the vector $\vec{e} = \vec{e}_{j_2}$ is removed from the set E , and in line 6,

$$\vec{y} = \vec{z}_0 + \vec{e} = \vec{z}_0 + \vec{e}_{j_2} = \vec{z}_2.$$

We have

$$\{\pm(Y - \vec{y})\} \subseteq \{\pm(\mathcal{Y}_0 - \vec{z}_2)\} \subseteq \mathcal{E}^{est}$$

since $Y \subset \mathcal{Y}_0$, so line 8 must be executed. This takes us to the next recursion, with E containing the offset vectors $\vec{e}_{j_3}, \dots, \vec{e}_{j_m}$, and $Y \cup \{\vec{y}\} = \{\vec{z}_0, \vec{z}_1, \vec{z}_2\}$.

m^{th} –**Recursion:** At this recursion level, E contains the element \vec{e}_{j_m} and $Y = \{\vec{z}_0, \vec{z}_1, \dots, \vec{z}_{m-1}\}$. Similar to above, we know that at some iteration of the while loop, at line 5, the vector $\vec{e} = \vec{e}_{j_m}$ is removed from the E , and in line 6,

$$\vec{y} = \vec{z}_0 + \vec{e} = \vec{z}_0 + \vec{e}_{j_m} = \vec{z}_m.$$

Moreover

$$\{\pm(Y - \vec{y})\} \subseteq \{\pm(\mathcal{Y}_0 - \vec{z}_m)\} \subseteq \mathcal{E}^{est}$$

since $Y \subset \mathcal{Y}_0$. Therefore line 8 has to be executed, and this take us to next recursion with all the vectors (53) removed from E and $Y \cup \{\vec{y}\} = \{\vec{z}_0, \vec{z}_1, \dots, \vec{z}_{m-1}, \vec{z}_m\}$.

$(m+1)^{\text{th}}$ –**Recursion:** At this recursion level since

$$Y = \{\vec{z}_0, \vec{z}_1, \dots, \vec{z}_m\} = \mathcal{Y}_o$$

and since $\mathcal{E}^{est} = \mathcal{E}(\mathcal{Y}_o)$, line 2 is executed and the recursion returns $\mathcal{Y}^{est} = Y$, which is a non-empty set.

This contradicts our assumption $\mathcal{Y}^{est} = \emptyset$. Thus, we conclude (51) returns a non-empty \mathcal{Y}^{est} .

Acknowledgment

This work is supported in part by the NSF grant DMS1510429 and by the NSF Grant DMS-1439786, while Liliana Borcea was in residence at the Institute for Computational and Experimental Research in Mathematics in Providence, RI, during the Fall 2017 semester.

References

- [1] J. M. Beckers, *Adaptive Optics for Astronomy: Principles, Performance, and Applications*, Annual Review of Astronomy and Astrophysics. 31 (1), 1993, pp. 13-62.
- [2] N. Bleistein, J. K. Cohen and W. John Jr. *Mathematics of multidimensional seismic imaging, migration, and inversion*, Vol. 13. Springer Science & Business Media, 2013.
- [3] L. Borcea, J. Garnier, G.C. Papanicolaou and C. Tsogka, *Enhanced statistical stability in coherent interferometric imaging*, Inverse problems, 27, 2011, p. 085004.
- [4] L. Borcea, G.C. Papanicolaou and C. Tsogka, *Adaptive interferometric imaging in clutter and optimal illumination*, Inverse Problems, 22, 2006, p. 1405.

- [5] L. Borcea, G.C. Papanicolaou and C., Tsogka, *Asymptotics for the space-time Wigner transform with applications to imaging*, Stochastic Differential Equations: Theory and Applications. P.H. Baxendale and S.V. Lototsky, Editors, Interdisciplinary Mathematical Sciences, vol 2, World Scientific, 2007.
- [6] L. Borcea and I. Kocyigit, *Resolution analysis of imaging with ℓ_1 optimization*, SIAM Journal on Imaging Sciences, 8, 2015, pp. 3015-3050.
- [7] L. Borcea and I. Kocyigit, *Imaging in random media with convex optimization*, SIAM Journal on Imaging Sciences 10.1, 2017, pp. 147-190.
- [8] A. Chai, M. Moscoso, and G. Papanicolaou, *Robust imaging of localized scatterers using the singular value decomposition and ℓ_1 minimization*, Inverse Problems, 29, 2013, p. 025016.
- [9] A. Chai, M. Moscoso, and G. Papanicolaou, *Imaging strong localized scatterers with sparsity promoting optimization*, SIAM Journal on Imaging Sciences, 7, 2014, pp. 1358-1387.
- [10] J.C. Curlander and R.N. McDonough, *Synthetic aperture radar*, New York, NY, USA: John Wiley & Sons, 1991.
- [11] L. Devroye, *Nonuniform random variate generation*, Handbooks in operations research and management science, 13 (2006), pp. 83-121.
- [12] A. C. Fannjiang, T. Strohmer, and P. Yan, *Compressed remote sensing of sparse objects*, SIAM Journal on Imaging Sciences, 3, 2010, pp. 595-618.
- [13] L.A. Gorham, B.D. Rigling and E.G. Zelnio, *A comparison between imaging radar and medical imaging polar format algorithm implementations*, Proceedings of SPIE, 6568, 65680K, 2007.
- [14] J. A. Jackson and R. L. Moses and E. G. Zelnio and F. D. Garber, *Feature extraction algorithm for 3 D scene modeling and visualization using monostatic SAR*, in Proceedings of SPIE, Vol. 6237, No. 1, 2006, pp. 55-66.
- [15] R. O. Nielsen, *Sonar signal processing*, Artech House, Inc., 1991.
- [16] P. Kutchment and L. Kunyansky, *Mathematics of thermoacoustic and photoacoustic tomography*, Handbook of Mathematical Methods in Imaging, O. Scherzer, ed., Springer-Verlag, 2010, pp. 817-866.
- [17] S.M. Rytov, Y.A. Kravtsov, and V.I. Tatarskii, *Principles of statistical radiophysics 4. Wave Propagation through random media*, Springer Verlag, Berlin, 1989.
- [18] T. L. Szabo, *Diagnostic ultrasound imaging: inside out*, Academic Press, 2004.
- [19] M. C. W. van Rossum, T. M. Nieuwenhuizen, *Multiple scattering of classical waves: microscopy, mesoscopy, and diffusion*, Biomedical Optics Express 71 (1999) 313-371.

- [20] T. Eren and O. K. Goldenberg and W. Whiteley and Y. R. Yang and A. S. Morse and B. D. O. Anderson and P. N. Belhumeur, *Rigidity, computation, and randomization in network localization*, IEEE Infocom, 2004.
- [21] A. Javanmard and A. Montanari, *Localization from Incomplete Noisy Distance Measurements* Foundations of Computational Mathematics, 2013.